Source Parameters of Earthquakes in Eastern and Western North America Based on Finite-Fault Modeling

by Igor A. Beresnev and Gail M. Atkinson

Abstract   The ground motion from large earthquakes is often predicted based on finite-fault modeling, in which the fault plane is discretized into small independently rupturing subfaults; the radiation from all subfaults is summed at the observation point. Despite the success of the method in matching observed ground-motion characteristics, the physical interpretation of the subfaults has remained largely unclear, and a rationale for the choice of the subfault attributes has been lacking. Two key parameters—the subfault size and the maximum slip velocity on the fault—govern the amplitude of the source spectrum at intermediate and high frequencies, respectively. We determined these key source parameters, on an event-by-event basis, for all well-recorded moderate to large earthquakes in western North America (WNA) by fitting simulated to observed response spectra. We compare the values of these source parameters with those obtained previously for eastern North America (ENA) and the Michoacan, Mexico, earthquakes (a total of 26 modeled events).

We find that the characteristic subevent size increases linearly with moment magnitude in an apparently deterministic manner. The subevent size relationship obtained for WNA is not statistically different from that obtained for ENA. In both regions, the subevent size follows the trend of $\log \Delta l = -2 + 0.4 \, \mathbf{M}$ ($4 \leq \mathbf{M} \leq 8$), where Δl is the subfault size in km. This trend agrees well with independent studies by Somerville *et al.* (1999) and Aki (1992), in which the characteristic size of the patches ("asperities" or "barriers") on earthquake faults was determined. These results indicate that large earthquakes should be viewed as a sequence of smaller events that comprise the large rupture. Interestingly, the characteristic size of these constituent small events appears to be directly related to the size of the overall rupture.

The slip velocities determined for all 26 earthquakes vary in a narrow range from about 0.25 to 0.60 m/sec, with a mean of 0.40 m/sec and standard deviation of 0.09 m/sec. The slip velocities for the ENA events are distributed randomly over this range, while those for the WNA region appear to exhibit a decreasing trend with increasing magnitude. Our results indicate that a generic, region-independent earthquake source model for engineering prediction of strong ground motions can be developed.

Introduction

To adequately design an earthquake-resistant structure, engineers need to know the characteristics of the expected ground shaking for a given location. Ground motions are estimated by identifying the major regional faults (or source zones) and propagating seismic waves generated at these potential sources to the site of interest. While the gross path effects, such as geometric spreading and anelastic attenuation, can be predicted quite well on average from either empirical or theoretical models, there is much debate as to the nature of the seismic source radiation.

Both point-source and extended-source models are used in ground-motion modeling. Despite the popularity of the point-source model (introduced by Brune, 1970), the current emphasis in ground-motion prediction is shifting toward an extended, or finite-fault, source representation. The point-source approximation is clearly unable to characterize key features of ground motions from large earthquakes, such as their long duration and the dependence of amplitudes and duration on the azimuth to the observation point (source directivity).

Finite-fault effects contribute not only to the duration and directivity of ground motions, they also affect the shape of the spectra of seismic waves. The classic Fourier spectrum of ground acceleration near a point dislocation (an "ω^2"

spectrum) is given by the function $\omega^2/[1 + (\omega/\omega_0)^2]$, where ω is the angular frequency and ω_0 is the corner frequency (Aki, 1967; Brune, 1970). At low frequencies (below ω_0), the spectrum rises with frequency, whereas at high frequencies (above ω_0), the spectrum is constant. In the classic model, the corner frequency ω_0 is inversely proportional to the event size. The spectra from small to moderate earthquakes roughly follow the ω^2 model, demonstrating that the point-source representation works reasonably well for these events (e.g., Boore, 1983). However, the analysis of empirical databases, both in California and eastern North America, suggests that large events (generally, $\mathbf{M} \geq 6$) do not obey this simple spectral shape, especially at low to intermediate frequencies ($\sim$0.2–2 Hz), where they radiate less energy than is predicted by point-source models (e.g., Atkinson, 1993; Atkinson and Silva, 1997, 2000). This observation can be explained in terms of the finite spatial extent of large earthquake sources, as shown below.

A discrete finite-fault model of radiation is capable of reproducing the salient ground-motion characteristics of large earthquakes and has therefore been extremely popular over the past two decades. In this model, introduced by Hartzell (1978), the finite-fault plane is subdivided into elements (subfaults), and the radiation from a large earthquake is obtained as the sum of contributions from all elements, each of which acts as an independent (sub)source. In the typical implementation, the rupture starts at a hypocentral point on the fault and propagates radially from it, triggering the subfaults as it passes them. The fields from all subevents are geometrically delayed and added together at the observation point. Note that we assign the same meaning to subfaults and subevents in this article because, as we show, our subfaults are assigned a characteristic dimension that is representative of subevent size for the modeled fault plane. Engineering simulations of ground motions from significant seismic events have been performed primarily through such kinematic models (Kanamori, 1979; Irikura, 1983; Heaton and Hartzell, 1989; Somerville *et al.,* 1991; Hutchings, 1994; Tumarkin and Archuleta, 1994; Zeng *et al.,* 1994; also see the review of recent work in Beresnev and Atkinson, 1997).

Despite the apparent success of this method in reproducing observed ground-motion characteristics, its applicability has never been strictly justified and has remained heuristic in nature. Indeed, the approach assumes that a large earthquake is composed of independent events occurring on independently rupturing subfaults, which is not what follows from the representation theorem (e.g., Aki and Richards, 1980, their equation 14.7). The chief justification for the use of the discrete finite-fault model for ground-motion prediction has been that it appears to work and that it provides more realistic time series and spectra than those obtained from point-source models. A critically minded observer might ask, "What is the basis for the belief that a continuous earthquake rupture can be represented as a series of isolated, smaller events?" Should we consider this method a technical ploy, fortuitously leading to the right answer, or does it fundamentally reflect the way real earthquakes rupture? Answering these questions is important for engineering seismology and earthquake physics in general.

Apart from this apparent conceptual weakness, another problem that discrete finite-fault models have invariably faced is the lack of a practical recipe for the choice of the appropriate subfault attributes. Indeed, if the idea of discretization of a large earthquake into smaller subevents can be taken for granted, what is the size of those characteristic earthquakes that make up a large event? Is the latter composed of a thousand small patches or no more than a few moderate events? This problem has not gone unnoticed, and the technical solutions proposed to date have generally been based on the postulate of self-similarity, or the assumption that the spectra of the largest events follow the same ω^2 shape that is characteristic of smaller earthquakes. Simple summation rules, also prescribing the subfault size, have been developed to preserve the shape of spectra through different modeling scales (e.g., Joyner and Boore, 1986; Irikura and Kamae, 1994). Although technically attractive, such solutions cannot be considered satisfactory. There is no sound basis for the applicability of self-similar spectral behavior, which is strictly valid for point dislocations only, to the scales of large and great earthquakes. Furthermore, the self-similarity postulate contradicts empirical data even for moderate seismic events, and certainly for large events (e.g., Atkinson, 1993; Atkinson and Silva, 1997, 2000). In the absence of physically justified or well-calibrated rules for subfault-size selection, modelers have approached this aspect of ground-motion simulations on a rather *ad hoc* basis, often basing their selection on a particular aftershock record that happens to be available.

Intuitively, it appears quite natural that faults rupture as a sequence of breakage of small areas (asperities), rather than in a smooth and continuous manner, and this concept has a long history (e.g., Wyss and Brune, 1967; Papageorgiou and Aki, 1983). To clarify the terminology used in this article, we note that the analogy of our subfaults to the commonly used asperities is based on the definition of both as characteristic zones on the fault that form the salient features of radiation. The subsequent comparisons of the sizes of characteristic slip zones from different studies are based on this definition. If we accept that the faults rupture discretely, we can qualitatively explain why the discrete rupture process creates the observed deficit of energy at intermediate frequencies, relative to the ω^2 shape of an equivalent point source. The acceleration spectrum of ground motions from each small event decays quickly at frequencies below its corner frequency, which is high due to the small size of the subevent. However, at very low frequencies, the signals sum up coherently, boosting low-frequency energy. The net result is a spectrum that is relatively rich in radiated energy at the high- and low-frequency ends of the spectrum, with a sag in between (also see Beresnev and Atkinson, 1999, pp. 609–610, and their figure 3). Two parameters govern the

radiated spectral shape: (1) as shown by Beresnev (2001), the slip velocity on the fault controls the amplitude of the radiated spectrum at high frequencies; and (2) the subfault (asperity) size controls the location and depth of the spectral sag. Thus the subfault size is an important model parameter and cannot be arbitrarily chosen.

In our previous work (Beresnev and Atkinson, 1999), we calibrated the finite-fault radiation model against well-recorded earthquakes in eastern North America (ENA), determining the slip velocity and the subfault size for each modeled event. By matching the observed and simulated spectral levels, we found that the subfault size that provides the least simulation bias follows a simple linear relationship with earthquake magnitude. Thus, one of the essential simulation parameters is a well-constrained function of magnitude, significantly reducing ambiguity in assigning the size of a subevent to the modeled earthquake.

In the present work, we extend the finite-fault model calibration to seventeen well-recorded moderate-to-large earthquakes in western North America (WNA), which cover the magnitude range from 4.7 to 7.3. The earthquakes in the moderate to large magnitude range are of most importance for engineering applications. We also provide comparison of source parameters derived for the WNA and the earlier modeled ENA events.

Simulation Method and Database

We use the stochastic finite-fault simulation technique, implementing the concept of fault discretization wherein subevents are represented as stochastic point sources. The detailed description of the method and references to the works on which it is based are given by Beresnev and Atkinson (1997, 1998a); here we provide a general method outline. Every subfault is assigned an average ω^2 spectrum with a stochastic component superimposed on it; this reproduces the realistic quasi-random shape of observed ground-acceleration time histories. The randomization of the spectrum is done according to the procedure defined by Boore (1983); a Gaussian noise spectrum with unit spectral amplitude is multiplied by the underlying ω^2 point-source model spectrum. The number of subsources summed is prescribed by the total magnitude (seismic moment) of the target event. Even though each elementary source radiates an ω^2 spectrum, the result of the summation of all radiated fields under the conservation-of-moment constraint does not lead to the same spectral shape; a spectral sag is created by the summation process as described previously (see also Beresnev and Atkinson, 1997; Atkinson and Silva, 1997).

The two free parameters of the simulations are the maximum slip velocity (v_m) on the fault and the subfault size (Δl), controlling the amplitude of the simulated finite-fault spectrum at high and intermediate frequencies, respectively. These two parameters, combined with the total moment of the simulated event, completely define the shape of the source spectrum. For each event, the modeling error (also

termed the simulation bias)—defined by the logarithm of the ratio of the observed to simulated response spectrum, averaged over all stations—is calculated for a given set of model parameters, over the frequency range from 0.2 to 13 Hz (or over the actual frequency range available from the original recordings). The slip velocity and Δl are then iteratively adjusted, using a grid-search approach, to minimize the error over the entire frequency band. We chose to simulate and calculate bias for the response spectra, as it is the characteristic of ground motions most relevant for engineering applications. All simulations use the FORTRAN code FINSIM, written and publicly released by the authors (Beresnev and Atkinson, 1998a). All output- and input-parameter files used in this study, as well as a copy of the code, are freely available from the authors.

The list of all modeled WNA earthquakes is given in Table 1, along with the fault geometries and event-specific simulation parameters. We use the published fault rupture dimensions if they are available. Otherwise (for most moderate events), we use the empirical relationship between the rupture area and the moment magnitude developed by Wells and Coppersmith (1994; their table 2A and figure 16a): log (RA) $= -3.49 + 0.91$ **M**, where RA is the rupture area in km^2. All observed data were obtained from the response-spectral database compiled by Pacific Engineering & Analysis (courtesy of W. J. Silva). This collection of data includes spectra of reliable corrected earthquake records in the usable frequency range, which facilitates their comparison with the results of simulations. The only exception is the Northridge earthquake, for which the earlier modeling results of Beresnev and Atkinson (1998b) were used.

To avoid complications related to the effects of local soil conditions on the amplitudes of ground motions, only data recorded on sites categorized as rock were used (Geomatrix Classes A and B, or typical shear-wave velocity of about 600 m/sec averaged over the top 30 m). Only events that had at least four rock recordings were selected for modeling. The list of all modeled stations for each event is given in Table 2. Table 3 lists the geographic coordinates, location, owner agency, and Geomatrix site class for these stations in alphabetical order. The generic modeling parameters common for all events are summarized in Table 4. Note that all sites are assumed to contain the generic WNA rock amplification described by Boore and Joyner (1997). A simplified form of the distance-dependent duration term ($0.1R$) was adopted from the results of Raoof *et al.* (1999, their figure 8).

Modeling Results

Model Bias

Figure 1 presents the mean modeling bias for all 17 simulated WNA events. The biases were determined at a series of frequencies equally spaced on the logarithmic scale, which are marked with the black circles (see details in figure caption). The $\pm$ one standard deviation and 95% confidence

Table 1
WNA Events and Finite-Fault Parameters

Event Name	Date (mm/dd/yy)	Coordinates of Epicenter (deg)	Moment Magnitude (M)	Strike and Dip (deg)	Depth to Upper Edge (km)	Number of Stations	References	Fault Length and Width (km)	Subfault Size (km)	Ratio of Fault to Subfauls Size	Maximum Slip Velocity (m/sec)
Oroville aftershock	08/08/75	39.50, −121.51	4.7	357, 46	6	4	Fletcher et al. (1984)	2×2	0.3	7	0.49
Coalinga aftershock	05/09/83	36.246, −120.300	5.0	136, 44	12	10	Eaton (1990)	3×3	1.5	2	0.54
Mammoth Lakes aftershock	06/11/80	37.509, −119.043	5.0	105, 70	3	4	Archuleta et al. (1982)	3×3	0.5	6	0.46
Coalinga aftershock	07/09/83	36.251, −120.400	5.2	18, 41	9	9	Eaton (1990)	4×4	1.3	3	0.49
Livermore	01/27/80	37.74, −121.74	5.4	321, 70	12	7	Bolt et al. (1981)	4.5×4.5	2.25	2	0.43
Lytle Creek	09/12/70	34.27, −117.54	5.4	55, 60	8	7	http://smdb.crustal.ucsb.edu	5×5	1.25	4	0.49
Coalinga aftershock	07/22/83	36.241, −120.409	5.8	355, 38	3	7	Eaton (1990)	8×8	2.7	3	0.38
Livermore	01/24/80	37.85, −121.82	5.8	167, 85	0	5	Bolt et al. (1981)	7×7	3.5	2	0.35
North Palm Springs	07/08/86	33.915, −116.530	6.0	287, 46	4	12	Hartzell (1989)	16.5×12	1.5	10	0.51
Whittier Narrows	10/01/87	34.098, −119.015	6.1	280, 30	12	26	Hartzell and Iida (1990)	9×9	3.0	3	0.49
Chalfant Valley mainshock	07/21/86	37.62, −118.443	6.2	148, 55	1	4	Cockerham and Corbett (1987); Savage and Gross (1995)	15×9	3.0	4	0.30
Morgan Hill	04/24/84	37.309, −121.678	6.2	148, 90	1	8	Hartzell and Heaton (1986)	24×9	3.0	6	0.32
Coalinga	05/02/83	36.221, −120.292	6.4	145, 30	4	20	Eaton (1990); Stein and Ekström (1992)	15×15	5.0	3	0.35
San Fernando	02/09/71	34.28, −118.33	6.6	290, 50	0	23	Heaton (1982)	18×20	5.5	4	0.35
Northridge	01/17/94	34.43, −118.57	6.7	122, 40	5	28	Wald et al. (1996); Beresnev and Atkinson (1998b)	20×25	5.0	5	0.43
Loma Prieta	10/17/89	37.200, −122.030	7.0	128, 70	1.5	34	Wald et al. (1991)	40×20	10	3	0.43
Landers	06/28/92	34.095, −116.330	7.3	341, 90	0	9	Wald and Heaton (1994)	80×16	8	6	0.32

Table 2
Stations Modeled for Each Event*

Oroville Aftershock
DWR (6.5[†])   OR7 (6.7[†])   OR6 (8.6[†])   DJR (10.7[†])

Coalinga Aftershock 9 May 1983
OLF (12.1[†])   ATC (12.6[†])   CPL (12.6[†])   VEW (12.6[†])   COL (12.7[†])   PLM (12.7[†])   LLN (13.1[†])   OLC (13.3[†])
SGT (14.1[†])   CSU (20.3[†])

Mammoth Lakes Aftershock
COV (7.6[†])   XCV (9.1[†])   XMG (11.1[†])   XNM (12.3[†])

Coalinga Aftershock 9 July 1983
OLC (10.0[†])   TSM (10.4[†])   ATC (11.0[†])   ATP (11.0[†])   OLF (11.9[†])   OLP (11.9[†])   SKH (12.6[†])   PLM (14.0[†])
CSU (17.0[†])

Livermore 27 January 1980
LFA (3.6)   LMO (8.0)   DVD (12.9)   KOD (17.6)   SRM (21.7)   FRE (29.8)   HAY (31.0)

Lytle Creek
WTW (15.4[†])   CSM (20.6[†])   DCF (21.9[†])   CSD (23.7[†])   PUD (32.8[†])   SAD (45.9[†])   ORR (107.8[†])

Coalinga Aftershock 22 July 1983
OLC (8.2)   TSM (9.2)   CSU (9.7)   OLF (10.9)   OLP (10.9)   PLM (12.2)   SKH (12.2)

Livermore 24 January 1980
DVD (12.9)   KOD (17.6)   SRM (21.7)   FRE (29.8)   HAY (31.0)

North Palm Springs
H10 (25.8)   HCP (34.9)   CFR (35.3)   ARS (43.8)   A01 (45.6)   ATL (55.4)   H02 (57.6)   H01 (63.3)
RVA (71.1)   PLC (71.9)   TEM (73.2)   LMR (73.7)

Whittier Narrows
GRN (9.0)   SOR (10.5)   JOS (10.8)   NHO (11.9)   GRV (12.1)   MTW (21.2)   ORN (23.0)   BRL (23.3)
WON (24.6)   CBN (26.8)   FAR (28.5)   SUL (29.3)   SER (30.1)   CHA (32.6)   SEC (32.6)   ANG (34.5)
PAC (37.9)   SUN (38.6)   LAS (46.3)   VAS (52.4)   VIR (53.3)   RIV (56.8)   WPA (60.0)   MAL (65.3)
CSH (70.9)   CSR (78.3)

Chalfant Valley
PAR (23.0)   LVD (33.4)   TIN (40.6)   MAM (50.8)

Morgan Hill
CYC (0.1)   G06 (11.8)   GMR (14.0)   G01 (16.2)   GIL (16.2)   CLS (22.7)   FMS (31.4)   LOB (44.1)

Coalinga
PGD (24.6)   SCN (27.7)   Z11 (28.4)   SC4 (29.6)   Z08 (29.6)   Z15 (29.9)   SC3 (31.8)   Z09 (31.9)
VYC (32.3)   Z06 (32.8)   Z04 (34.3)   SC2 (34.4)   VC4 (34.6)   PG2 (36.6)   VC5 (37.1)   TM3 (38.4)
PG3 (38.8)   TM2 (40.5)   PG4 (41.7)   PG5 (43.7)

San Fernando
PCD (2.8)   PSL (19.1)   L12 (20.3)   L09 (23.5)   L04 (24.2)   CRR (24.9)   SAD (27.0)   FSD (27.5)
FIR (29.1)   PPP (38.9)   SOD (58.1)   WTW (60.3)   FTJ (64.1)   CND (66.4)   TEH (68.0)   CSM (86.6)
CSP (87.6)   ISD (113.0)   MA2 (113.0)   MA3 (113.0)   MA1 (115.0)   SON (122.0)   C08 (223.0)

Loma Prieta
CLS (5.1)   LGP (6.1)   BRN (10.3)   G01 (11.2)   GIL (11.6)   LOB (17.9)   G06 (19.9)   ANA (21.4)
CYC (21.8)   GMR (24.2)   SGI (30.6)   SG3 (34.7)   SLC (36.3)   WDS (39.9)   MSJ (43.0)   FM2 (43.4)
MCH (44.8)   A09 (46.9)   A07 (47.7)   A10 (47.8)   BES (49.9)   A3E (57.1)   SSF (68.2)   DMH (77.0)
PJH (78.3)   RIN (79.7)   YBI (80.6)   PHT (81.6)   TLH (82.0)   PRS (83.1)   BRK (83.6)   CFH (84.4)
GGB (85.1)   PTB (88.6)

Landers
LUC (1.1)   29P (42.2)   SIL (51.7)   AMB (69.2)   PUE (95.9)   RIV (96.1)   MEL (126.4)   GLN (162.6)
VIR (194.1)

*Stations are listed in order of increasing distance from the fault. The number in parentheses after station code is the closest distance to the fault plane
[†]Hypocentral distances instead of closest distances.
Source: Pacific Engineering & Analysis strong-motion database. Refer to Beresnev and Atkinson (1998b, Table 1) for a list of modeled stations for the Northridge earthquake.

Table 3
Station Parameters*

Station Code	Latitude (°)	Longitude (°)	Location	Owner	Geomatrix Site Class[†]
29P	34.021	−116.009	Twentynine Palms	CDMG	A
A01	33.630	−116.847	Anza–Red Mountain	USGS	A
A07	37.484	−122.313	APEEL 7–Pulgas	CDMG	A
A09	37.470	−122.320	APEEL 9–Crystal Springs Res	USGS	A
A10	37.465	−122.342	APEEL 10–Skyline	CDMG	A
A3E	37.657	−122.061	APEEL 3E Hayward CSUH	CDMG	A
AMB	34.560	−115.743	Amboy	CDMG	B
ANA	37.166	−121.628	Anderson Dam (L abut)	USGS	A
ANG	34.39	−118.079	Mill Creek, Angeles Nat For	USC	B
ARS	33.568	−116.510	Santa Rosa Mountain	USGS	A
ATC	36.233	−120.333	Anticline Ridge free-field	USGS	A
ATL	33.47	−116.64	Anza–Tule Canyon	USGS	A
ATP	36.233	−120.333	Anticline Ridge pad	USGS	A
BES	37.512	−122.308	Belmont–Envirotech	CDMG	A
BRK	37.876	−122.249	Berkeley LBL	CDMG	A
BRL	33.889	−117.926	Brea Dam (L abut)	USGS	B
BRN	37.047	−121.985	BRAN	UCSC	A
C08	35.671	−120.359	Cholame–Shandon Array #8	USGS	B
CBN	33.916	−117.842	Carbon Canyon Dam (L abut)	USGS	A
CFH	37.778	−122.513	SF–Cliff House	CDMG	A
CFR	33.738	−116.838	Cranston Forest Station	USGS	B
CHA	34.086	−118.481	LA–Chalon Rd	USC	B
CLS	37.05	−121.803	Corralitos	CDMG	B
CND	33.92	−117.84	Carbon Canyon Dam	ACOE	A
COL	36.275	−120.306	Oil Fields–Skunk Hollow	CDMG	A
COV	37.614	−118.831	Convict Lakes	USGS	B
CPL	36.209	−120.292	Anticline Ridge–Palmer Ave	CDMG	B
CRR	34.564	−118.642	Castaic–Old Ridge Route	CDMG	B
CSD	34.31	−117.3	Cedar Springs Pumphouse	CDWR	B
CSH	34.459	−118.65	Castaic–Hasley Canyon	CDMG	B
CSM	34.275	−117.335	Cedar Springs, Allen Ranch	CDWR	A
CSP	34.31	−117.3	Cedar Spring–Pump	CDWR	B
CSR	34.564	−118.642	Castaic–Old Ridge Route	CDMG	B
CSU	36.121	−120.397	Sulphur Baths (temporary)	CDMG	A
CYC	37.118	−121.55	Coyote Lake Dam (SW abut)	CDMG	A
DCF	34.210	−117.330	Devil's Canyon	CDWR	A
DJR	39.424	−121.521	Johnson Ranch	CDMG	B
DMH	37.740	−122.432	SF–Diamond Heights	CDMG	B
DVD	37.617	−121.746	Del Valle Dam (toe)	CDWR	B
DWR	39.510	−121.505	DWR garage	CIT	A
FAR	34.089	−118.435	LA–N Faring Rd	USC	B
FM1	37.53	−121.919	Fremont–Mission San Jose	CDMG	B
FM2	37.535	−121.929	Fremont–Emerson Court	USGS	B
FRE	37.53	−121.919	Fremont–Mission San Jose	CDMG	B
FSD	34.460	−118.753	Santa Felicia Dam (Outlet)	CDMG	A
FTJ	34.870	−118.900	Fort Tejon	USGS	B
FTR	34.704	−118.426	Fairmont Dam	CDMG	A
G01	36.973	−121.572	Gilroy Array #1	CDMG	A
G06	37.026	−121.484	Gilroy Array #6	CDMG	B
GGB	37.806	−122.472	Golden Gate Bridge	USGS	A
GIL	36.973	−121.568	Gilroy Gavilan Coll.	CDMG	B
GLN	34.235	−118.366	Sun Valley–Glenoaks	USC	B
GMR	37.033	−121.434	Gilroy Array #7	CDMG	B
GRN	34.091	−118.093	San Gabriel–E Grand Av	USC	A
GRV	34.05	−118.114	Garvey Res.–Control Bldg	USGS	B
H01	33.599	−117.132	Murrieta Hot Springs	CDMG	A
H02	33.64	−117.094	Winchester Bergman Ran	CDMG	A
H10	33.851	−116.852	Silent Valley–Poppet F	CDMG	A
HAY	37.657	−22.061	APEEL 3E Hayward CSUH	CDMG	A

(*continued*)

Table 3
Continued

Station Code	Latitude (°)	Longitude (°)	Location	Owner	Geomatrix Site Class[†]
HCP	33.676	−116.68	Hurkey Creek Park	USGS	B
ISD	35.65	−118.47	Isabella Dam (Aux abut)	ACOE	A
JOS	33.944	−118.087	Santa Fe Springs–E Joslin	USC	B
KOD	37.729	−121.928	San Ramon–Eastman Kodak	CDMG	B
L04	34.642	−118.481	Lake Hughes #4	USGS	A
L09	34.610	−118.560	Lake Hughes #9	USGS	A
L12	34.510	−118.560	Lake Hughes #12	CDMG	B
LAS	34.046	−118.637	Malibu–Las Flores Canyon	USC	B
LFA	37.753	−121.773	Livermore–Fagundas Ranch	CDMG	B
LGP	37.172	−122.010	LGPC	UCSC	A
LLN	36.211	−120.263	Temporary	USGS	A
LMO	37.819	−121.795	Livermore–Morgan Terr Park	CDMG	A
LMR	33.852	−117.451	Lake Mathews Dike Toe	CDMG	A
LOB	37.001	−122.06	UCSC Lick Observatory	CDMG	A
LUC	34.568	−116.612	Lucerne	SCE	A
LVD	37.588	−118.705	Long Valley Dam (Downstr)	CDMG	A
MA1	35.	−119.48	Maricopa Array #1	CDWR	B
MA2	35.04	−119.43	Maricopa Array #2	CDWR	B
MA3	35.08	−119.4	Maricopa Array #3	CDWR	B
MAL	34.013	−118.8	Malibu–Point Dume Sch	CDMG	B
MAM	37.638	−118.893	Mammoth Lakes Sheriff Subst.	CDMG	B
MCH	36.597	−121.897	Monterey City Hall	CDMG	A
MEL	34.150	−117.939	Duarte–Mel Canyon Rd	USC	B
MSJ	37.530	−121.919	Fremont–Mission San Jose	CDMG	B
MTW	34.224	−118.057	Mt Wilson–CIT Seis Sta	CDMG	A
NHO	34.1	−117.974	Baldwin Park–N Holly	USC	B
OLC	36.229	−120.360	Oil City	USGS	B
OLF	36.247	−120.314	Oil Fields Fire Station	USGS	A
OLP	36.247	−120.314	Oil Fields Fire Station-pad	USGS	A
OR6	39.449	−121.490	Summit Ave	CDMG	A
OR7	39.484	−121.510	Nelson Ranch	CDMG	B
ORN	33.935	−117.883	Orange Co. Reservoir	USGS	B
ORR	34.564	−118.642	Castaic–Old Ridge Route	CDMG	B
PAC	34.288	−118.375	Pacoima Kagel Canyon	CDMG	B
PAR	37.481	−118.602	Bishop–Paradise Lodge	CDMG	A
PCD	34.334	−118.396	Pacoima Dam	CDMG	B
PG2	35.812	−120.391	Parkfield–Gold Hill 2W	CDMG	B
PG3	35.796	−120.411	Parkfield–Gold Hill 3W	CDMG	B
PG4	35.785	−120.444	Parkfiled–Gold Hill 4W	CDMG	B
PG5	35.77	−120.477	Parkfield–Gold Hill 5W	CDMG	B
PGD	35.973	−120.467	Parkfield–Vineyard Cany 2E	CDMG	A
PHT	37.790	−122.429	SF–Pacific Heights	CDMG	A
PJH	37.823	−122.233	Piedmont Jr High	CDMG	A
PLC	33.324	−116.683	Puerta La Cruz	CDMG	B
PLM	36.209	−120.292	Palmer Ave	USGS	B
PPP	34.508	−117.922	Pearblossom Pump	CDWR	B
PRS	37.792	−122.457	SF–Presidio	CDMG	A
PSL	34.150	−118.170	Pasadena–Old Seismo Lab	USGS	A
PTB	37.822	−122.527	Point Bonita	CDMG	A
PUD	34.091	−117.808	Puddingstone Dam (abutment)	CDMG	B
PUE	33.324	−116.683	Puerta La Cruz	CDMG	B
RIN	37.786	−122.391	SF–Rincon Hill	CDMG	A
RIV	33.951	−117.446	Riverside Airport	CDMG	B
RVA	33.951	−117.446	Riverside Airport	CDMG	B
SAD	34.19	−118.02	Santa Anita Dam	LAFC	A
SC2	35.81	−120.282	Parkfield–Stone Corral 2E	CDMG	A
SC3	35.833	−120.27	Parkfield–Stone Corral 3E	CDMG	A
SC4	35.855	−120.281	Parkfield–Stone Corral 4E	CDMG	A
SCN	36.034	−120.59	Slack Canyon	CDMG	A

Table 3
Continued

Station Code	Latitude (°)	Longitude (°)	Location	Owner	Geomatrix Site Class[†]
SEC	34.005	−118.485	Santa Monica–Second St	USC	B
SER	33.821	−117.818	Villa Park–Serrano Ave	USC	B
SG3	36.753	−121.395	SAGO South–Surface	CDMG	B
SGI	36.765	−121.446	Hollister–SAGO Vault	USGS	A
SGT	36.237	−120.381	Temporary	USGS	A
SIL	33.851	−116.852	Silent Valley–Poppet Flat	CDMG	A
SKH	36.275	−120.306	Skunk Hollow	USGS	A
SLC	37.419	−122.205	Palo Alto–SLAC Lab	USGS	A
SOD	34.17	−117.68	Upland–San Antonio Dam	ACOE	A
SON	33.37	−117.56	San Onofre–So Cal Edison	SCE	B
SOR	34.064	−117.952	West Covina–S Orange	USC	B
SRM	37.780	−121.980	San Ramon Fire Station	CDMG	B
SSF	37.675	−122.388	So. San Francisco, Sierra Pt.	CDMG	A
SUL	34.235	−118.366	Sun Valley–Sunland	USC	B
SUN	34.042	−118.553	Pacific Palisades–Sunset	USC	B
TEM	33.496	−117.149	Temecula Fire Station	CDMG	B
TEH	34.942	−118.827	Techachapi Pump	CDWR	A
TIN	37.054	−118.229	Tinemaha Res. free field	CDMG	A
TLH	37.803	−122.408	SF–Telegraph Hill	CDMG	A
TM2	35.751	−120.259	Parkfield–Cholame 2E	CDMG	B
TM3	35.77	−120.247	Parkfield–Cholame 3E	CDMG	A
TSM	36.249	−120.343	Transmitter Hill	USGS	A
VAS	34.492	−118.327	Vasquez Rocks Park	CDMG	A
VC4	35.905	−120.55	Parkfield–Vineyard Cany 4W	CDMG	B
VC5	35.885	−120.565	Parkfield–Vineyard Cany 5W	CDMG	B
VEW	36.211	−120.313	Temporary	USGS	A
VIR	34.151	−118.696	Calabasas–N Las Virg	USC	B
VYC	35.922	−120.534	Parkfield–Vineyard Cany 3W	CDMG	A
WDS	37.429	−122.258	Woodside	CDMG	B
WON	34.114	−118.38	LA–Wonderland Ave	USC	A
WPA	34.024	−118.787	Malibu–W Pacific Cst Hwy	USC	B
WTW	34.361	−117.633	Wrightwood–6074 Park Dr	USGS	B
XCV	37.59	−118.850	Convict Lakes	USC	B
XMG	37.553	−118.794	McGree Creek	USC	A
XMM	37.639	−118.863	Mammoth Elementary School	USC	B
YBI	37.807	−122.361	Yerba Buena Island	CDMG	A
Z04	35.836	−120.395	Parkfield–Fault Zone 4	CDMG	B
Z06	35.859	−120.42	Parkfield–Fault Zone 6	CDMG	B
Z08	35.878	−120.381	Parkfield–Fault Zone 8	CDMG	B
Z09	35.879	−120.445	Parkfield–Fault Zone 9	CDMG	B
Z11	35.896	−120.398	Parkfield–Fault Zone 11	CDMG	B
Z15	35.921	−120.481	Parkfield–Fault Zone 15	CDMG	B

*Source: Pacific Engineering & Analysis strong-motion database.
[†]A, rock; B, shallow (stiff) soil.

interval of the mean are also indicated. The bias for the Northridge earthquake was adopted from figure 5 of Beresnev and Atkinson (1998b). The modeling bias for most events is not statistically different from zero, considering the respective width of the confidence interval. A large bias is noted for the Mammoth Lakes aftershock; however, there were only four stations available for this event (Table 2). As an example of individual simulations, Figure 2 compares the model spectra to the observed spectra on a station-by-station basis for the Loma Prieta earthquake, which has the largest number of stations. We acknowledge that discrepancies between the predictions and observations are significant for several stations. These discrepancies can be attributed to (1)

the simplicity of the model, and more importantly, (2) the effect of variable site response at our rock sites that was assumed to be close to unity. For example, the effect of site-specific amplification was found to play an important role in improving the fits between the simulated and observed spectra in previous applications of FINSIM (Berardi *et al.,* 2000; Castro *et al.,* 2001). On average, however, the method accurately reproduces the observations.

Subfault Size

Figure 3 plots the subfault size, determined for each simulated event, as a function of earthquake magnitude

Table 4
Generic Modeling Parameters of WNA Earthquakes

Parameter	Parameter Value
$Q(f)$	$180f^{0.45}$ (Raoof *et al.*, 1999)
Geometric spreading	$1/R$ ($R \leq 40$ km)
	$1/R^{0.5}$ ($R > 40$ km) (Raoof *et al.*, 1999)
Distance-dependent duration (sec)	$T_0 + 0.1R$, where T_0 is the source duration and R is in km
Crustal amplification	Boore and Joyner (1997) WNA
Kappa (parameter of high-cut filer) (sec)	0.05
Stress parameters (bars)	50
Windowing function	Saragoni-Hart
Crustal shear-wave velocity (km/sec)	3.0–3.7 (depending on fault depth: Boore and Joyner, 1997)
Rupture velocity	$0.8 \times$ shear-wave velocity
Crustal density (g/cm^3)	2.6–2.8 (depending on fault depth: Boore and Joyner, 1997)
Fault-slip distribution	Uniform
Stochastic trials to generate response spectrum	3

(solid circles). The subfault size was calculated as the average of its length and width. In Figure 3, we combined the WNA data with the previously determined values of Δl for the ENA events (Beresnev and Atkinson, 1999); the latter are marked with the open circles. Also plotted is Δl for the **M** 8.1 Michoacan, Mexico, earthquake (Beresnev and Atkinson, 1998a). One of the principal conclusions of our ENA study was that there was a simple linear relationship between the best-fitting subfault size and the magnitude of the simulated earthquake (size of the rupture) (Beresnev and Atkinson, 1999). The WNA data fit well into this general trend. Figure 3 shows the linear regression determined separately for the WNA (including the Michoacan event) and ENA data (solid and dashed lines, respectively). The 95% confidence intervals are indicated for each line. The two regressions are statistically indistinguishable over the common magnitude range of the data (**M** < 7), in that the ENA confidence band lies entirely within that of the WNA data. The nearly total overlap appears to persist up to **M** 8 as well, although there are few data points to constrain the curves at large magnitudes. Figure 3 indicates that characteristic subevent size for both eastern and western North America earthquakes follows a very similar trend.

Using the results in Figure 3, we treat the WNA and ENA data as one statistical ensemble and determine the regression line using all 26 earthquakes. The combined data are presented in Figure 4 as solid circles. The regression equation is

$$\log \Delta l = -2 + 0.4\,\mathbf{M}, \quad 4 \leq \mathbf{M} \leq 8, \tag{1}$$

where Δl is the subfault size in km.

This equation, obtained after adding 16 WNA earthquakes, is identical to the one derived earlier from just the ENA events (with addition of the Northridge and Michoacan

events) (Beresnev and Atkinson, 1999, their equation 1). This indicates a notable uniformity of source processes throughout tectonically different regions over a wide range in magnitudes. The characteristic subevent size for all events follows a well-defined straight line (equation 1) in an apparently deterministic manner.

Our findings suggest that even relatively small events (**M** 4–5) appear to rupture discretely, although for small magnitudes the difference in spectral shape between the finite-fault and point-source representation is not dramatic. Since the size of the subevent increases with magnitude, the number of small events that make up the large event never grows too large. Table 1 shows the ratio of the size of the total ruptured zone to the size of a subevent for the modeled WNA earthquakes (sizes were determined as the average of fault lengths and widths). If we consider the combination of WNA and ENA events, for earthquakes varying in magnitude by nearly four units and in linear dimensions from about 1 to 145 km, the ratio of fault to subfault size varies in a fairly narrow range, between 2 and 10, with the larger events (**M** > 6) typically having higher ratios.

Two other studies approached the problem of determining the characteristic size of the rupture zone on earthquake faults from different points of view. Somerville *et al.* (1999) summarized distributions of slip on the fault for 15 significant crustal earthquakes around the world, obtained over the last two decades by various investigators through the inversion of long-period seismic data. To obtain those slip inversions, the data were typically low-pass filtered at 1 sec or so. The slip distributions were used to identify the size of patches on the fault that accommodated most of the slip. These patches, called "asperities" by Somerville *et al.* (1999), are functionally equivalent to the "subevents" in our investigation, in that these are the smaller areas on the fault whose consecutive ruptures form the large seismic event. We determined the sizes of the asperities from Table 4 of Som-
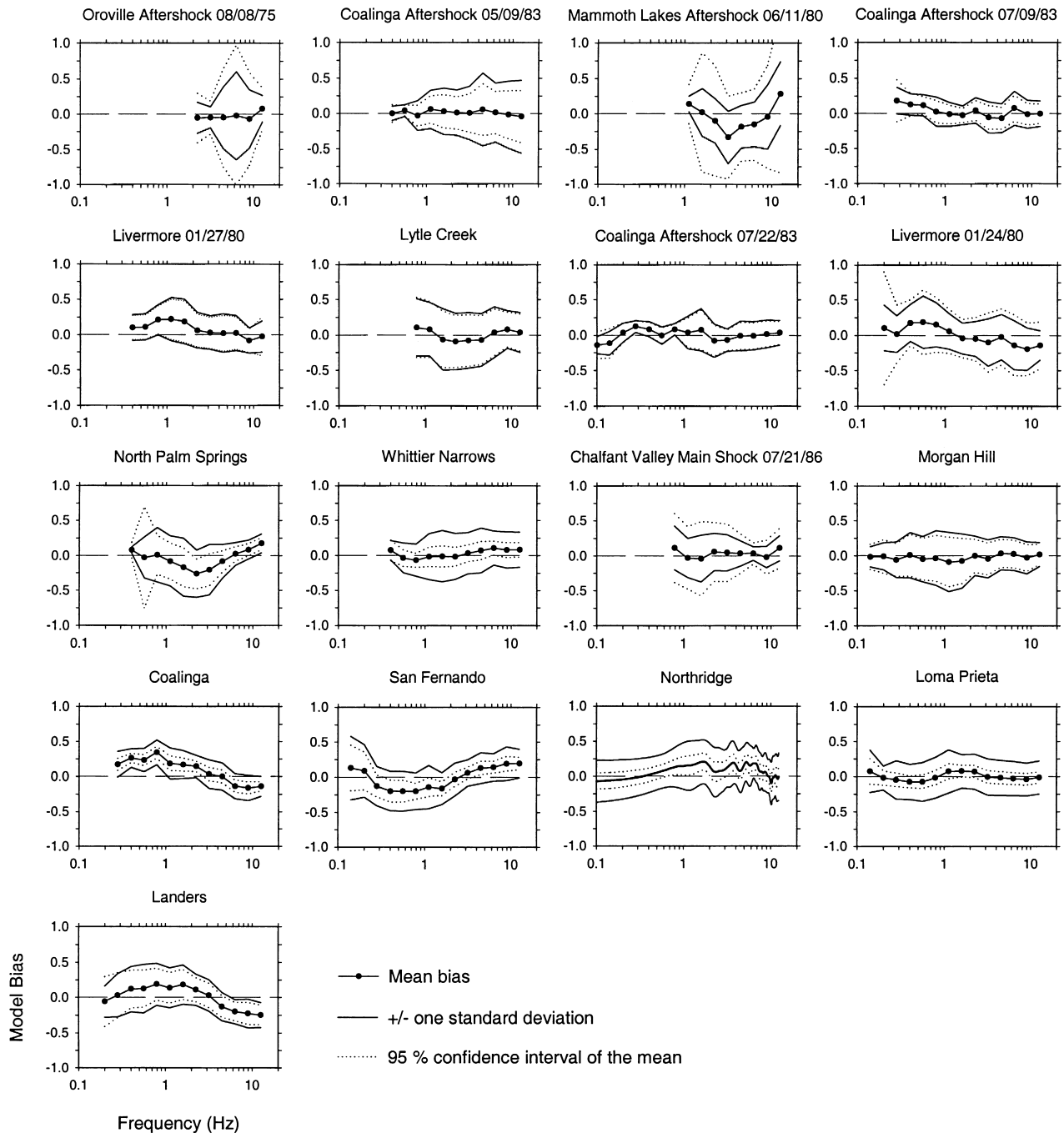
Figure 1.   Bias for all simulated WNA events. The bias is defined as the logarithm of the ratio of the observed to simulated response spectrum, averaged over all stations. The biases were determined at a series of frequencies equally spaced on the logarithmic scale (0.10, 0.14, 0.20, 0.28, 0.40, 0.56, 0.79, 1.12, 1.59, 2.24, 3.16, 4.47, 6.31, 8.92, and 12.6 Hz). Each panel also shows ± one standard deviation (thin solid lines) and 95% confidence interval of the mean (dotted lines).

erville *et al.* (1999) by calculating the average of the areas of asperities listed by the authors for each event and taking its square root. These sizes are shown as a function of earthquake magnitude in Figure 4 (open circles). These data nearly overlap the data from our study for earthquakes of magnitude 6 to 7; at larger magnitudes, Somerville *et al.*'s

characteristic subevent sizes tend to exceed the sizes from our investigation. The linear-regression equation drawn through the data of Somerville *et al.* (1999) is $\log \Delta l = -2 + 0.5 \, \mathbf{M}$ (thin solid line), which shows that the two sets of modeling results define a nearly identical trend. Our database is additionally constrained by the significant number of
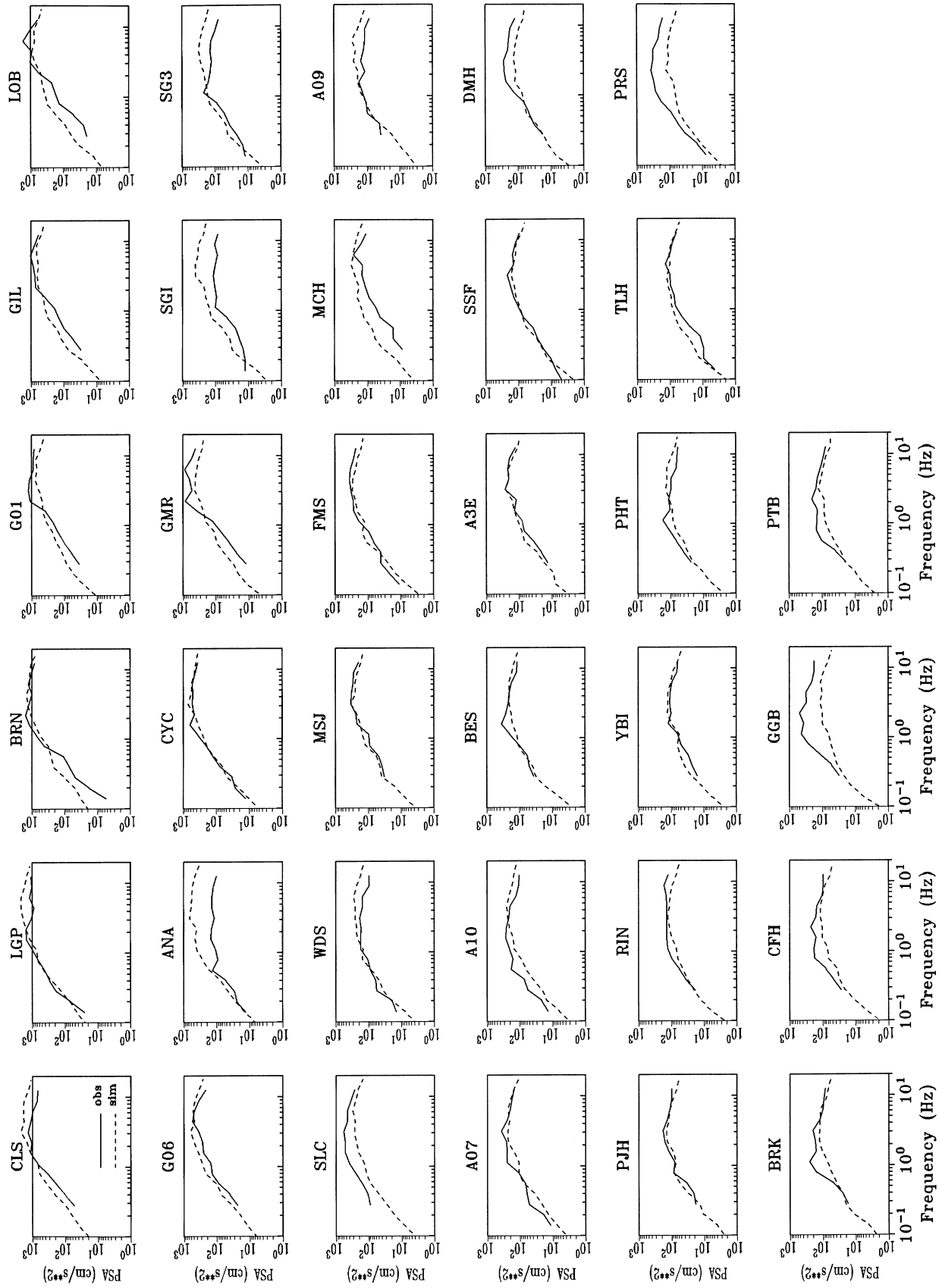
Figure 2. Observed and simulated 5% damped response spectra for the Loma Prieta earthquake (solid and dashed line, respectively). Stations are arranged in the order of increasing hypocentral distance (see Table 2).

705
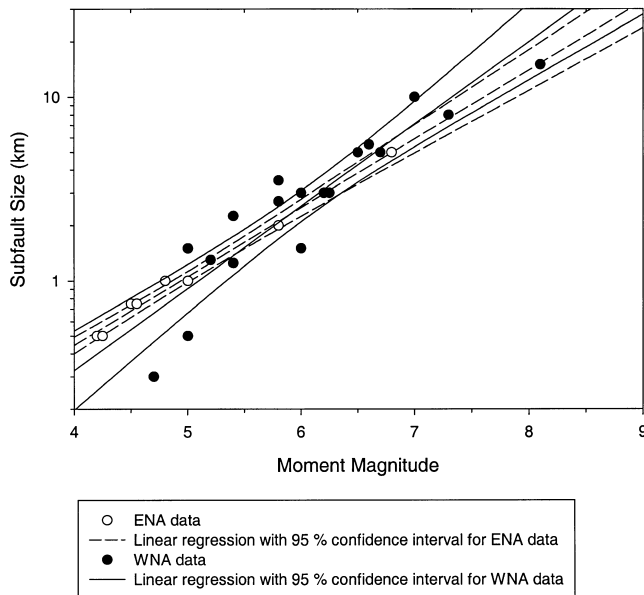
Figure 3.   Dependence of the finite-fault subfault size on earthquake magnitude. The data derived for the WNA and ENA earthquakes are plotted as solid and open circles, respectively. The linear regression lines to the WNA and ENA data are also shown, together with their 95% confidence intervals.
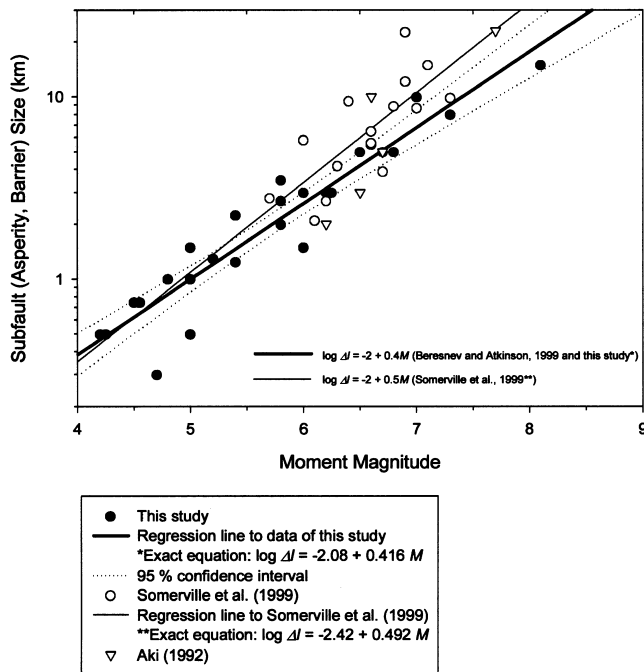
Figure 4.   Empirically derived dependencies of the size of characteristic rupture zone (subfault) on an earthquake fault on earthquake magnitude. The results of three independent studies are shown; the linear regression lines through two of them (our study and that of Somerville *et al.*, 1999) are indicated by the thick and thin solid lines, respectively.

Table 5
Comparison of Subevent Sizes of this Study, Asperity Sizes of Somerville *et al.* (1999), and Crack Diameters of Aki (1992) for Common Events

Event	This Study (km)	Somerville *et al.* (1999) (km)	Aki (1992) (km)
North Palm Springs	1.5	5.8	
Whittier Narrows	3.0	2.1	
Morgan Hill	3.0	2.7	
San Fernando	5.5	6.5	10.0
Northridge	5.0	3.9	
Nahanni (12-85)	5.0	8.9	
Loma Prieta	10.0	8.7	
Landers	8.0	9.9	
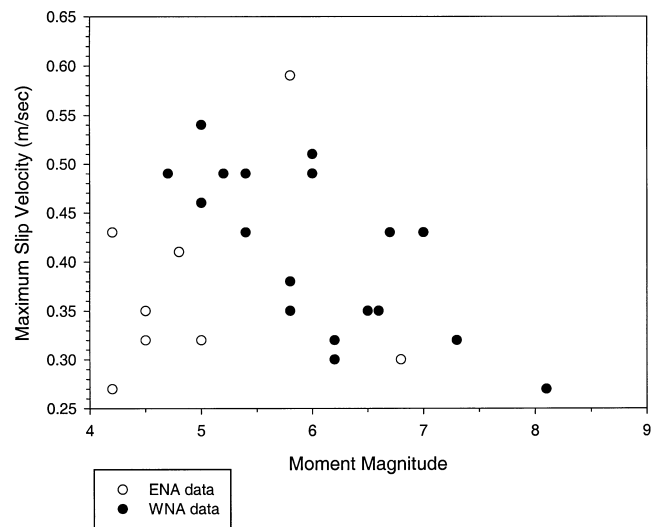
Figure 5.   Maximum slip velocities for 26 WNA and ENA events (from this study and that of Beresnev and Atkinson, 1999) as a function of moment magnitude. The WNA and ENA data are shown by the solid and open circles, respectively.

smaller-magnitude events (in the range of 4 to 6), which were not considered in Somerville *et al.*'s investigation.

It is significant that the subevent sizes in these two investigations were obtained in fundamentally different ways. While Somerville *et al.* (1999) used slip distributions obtained from a deterministic inversion of low-frequency data, our simulation matched both the low-frequency (deterministic) and high-frequency (stochastic) parts of the observed spectra using a stochastic approach. The subevent size thus appears to be a stable characteristic of an earthquake of specified magnitude, regardless of the underlying model assumptions.

The other relevant study is that of Aki (1992), who determined the characteristic diameter of circular cracks responsible for the high-frequency radiation from five major California earthquakes. Aki (1992) uses the term "barrier interval" for crack diameter, since the author's model rep-
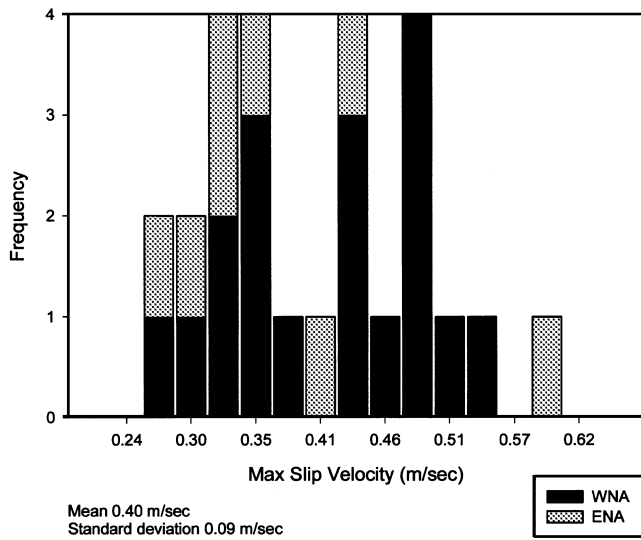
Figure 6. Histogram of maximum slip velocity on rupturing faults for the 26 WNA and ENA earthquakes. To distinguish between the WNA and RNA events, they are shown with two shades.

resents the rupture as an aggregate of cracks separated by unbroken barriers (the specific barrier model of Papageorgiou and Aki [1983]). The barrier interval thus has the meaning of the characteristic rupture size on an earthquake fault, which accords with the definition of subfaults in our study. The crack sizes of Aki (1992, figure 2) are indicated by inverted triangles in Figure 4. They agree with the trends established by both our study and that of Somerville *et al.* (1999), being closer to our regression line in the magnitude range of approximately 6–7, and closer to that of Somerville *et al.* (1999) at higher magnitudes. For direct comparison, the sizes of characteristic radiating zones from all three studies for the events in common are summarized in Table 5.

Slip Velocity

Simple reasoning suggests that the maximum velocity of slip v_m (hereafter simply called slip velocity) on the rupturing fault controls the amplitude of high-frequency radiation (Beresnev, 2001). Even intuitively, it is clear that the faster-growing dislocations produce more destructive ground motions, as opposed to the slow (aseismic creep) earthquakes, which may have the same moment but are not even felt at the surface. Mathematically, this is illustrated through the equivalence between corner frequency (ω_0) and v_m,

$$\omega_0 = e\frac{v_m}{u(\infty)}, \qquad (2)$$

where $u(\infty)$ is the total slip on the fault and e is the base of the natural logarithm (Beresnev, 2001, equation 3). From (2), assuming the ω^2 spectral shape, one obtains the scaling law for the high-frequency spectrum as

$$a_{hf}(\omega) \sim M_0 v_m^2, \qquad (3)$$

where M_0 is the seismic moment.

In some of our previous articles, we used the high-frequency radiation-strength factor (*s*) as a measure of the intensity of high-frequency spectral levels; *s* is also an input parameter to FINSIM. This factor serves as a proxy for the slip velocity and can be recalculated into v_m through the equation (Beresnev and Atkinson, 1999, equation 4; Beresnev, 2001, equation 19)

$$v_m = 0.618\, y\, \Delta\sigma\, s\, /(\rho\, \beta), \qquad (4)$$

where $\Delta\sigma$ is a constant expressing the average stress parameter (50 bars used in all simulations), *y* is the rupture propagation velocity as a fraction of shear-wave velocity β, and ρ is density. The slip velocities derived in this way from modeling the seventeen WNA events are tabulated in Table 1. Note that the quantity $\Delta\sigma$ has the physical meaning of the fault slip divided by fault dimension (multiplied by a constant) (Atkinson and Beresnev, 1997) and is well constrained to the assumed value on average (Kanamori and Anderson, 1975). It is not a factor controlling the shape of the spectrum of radiated waves, nor is it indicative of the high-frequency spectral level (see Atkinson and Beresnev [1997] for a discussion of the various definitions accorded to the term *stress drop*).

Figure 5 plots the inferred WNA slip velocities as a function of magnitude in comparison with the slip velocities obtained for ENA (Beresnev and Atkinson, 1999). The ENA data in Figure 5 (open circles) do not reveal a clear dependence on magnitude; their rather random character was one of the conclusions of Beresnev and Atkinson (1999). However, the WNA data (solid circles) suggest a trend of decreasing v_m with increasing earthquake size. This trend is our preliminary finding, which has yet to be independently confirmed. It is also not our goal in this article to speculate about the possible physical or tectonic cause of the slip velocity on faults decreasing with fault size.

If both WNA and ENA events are considered, the slip velocity appears to vary randomly over a small range, between 0.25 and 0.60 m/sec (radiation strength factor of 1.0 to 2.2). Figure 6 shows the histogram of slip-velocity distribution for all 26 events, with the WNA and ENA events distinguished by different shades. Assuming a normal distribution, the entire database suggests a mean velocity of 0.40 m/sec with the standard deviation of 0.09 m/sec. We acknowledge that these slip velocities fall in a surprisingly narrow range and that higher slip velocities are often inferred from other studies. For example, Wald *et al.* (1996) reported maximum slip velocity near the hypocenter of the 1994 Northridge earthquake of more than 4 m/sec, while slip velocities of greater than 1 m/sec are inferred from studies of the Loma Prieta earthquake (Steidl *et al.,* 1991; Wald *et al.,* 1991) and the Landers earthquake (Wald and Heaton, 1994; Cohee and Beroza, 1994), based on the maximum modeled slips and rise times. In comparison to our simplified ap-

proach, the detailed inversion studies referenced above look at slip in greater detail and may be capable of better resolving isolated patches of high slip. Our model may be reflecting a more smoothed picture of the slip velocity. On the other hand, detailed slip inversions necessarily contain their own intrinsic assumptions and trade-offs, and thus inferred slip velocities from these studies are also subject to significant uncertainty. To the extent of our knowledge, the most complete illustration of stunning uncertainties in obtaining slip inversions from observed data was published by Olson and Apsel (1982), who showed that details of the inverted slip distribution are virtually controlled by the assumed parameterization scheme and the adopted set of constraints on the inversion algorithm. Even their study, in our opinion, did not address all possible sources of ambiguity, and it is beyond the scope of this article to further elaborate on them. Interestingly, our relatively smooth and simple representation of slip appears to be capable of modeling the observed ground-motion amplitudes as accurately as more detailed methods. The issue of slip velocity on faults is an area of active investigation, and there is much more to be learned before truly definitive conclusions on slip velocities can be reached.

Even though the slip velocity appears to vary over a relatively small range around its mean of 0.40 m/sec, these variations lead to a substantial change in the amplitude of high-frequency radiation. This happens because the high-frequency spectral level is proportional to v_m^2 (equation 3). We conclude that the maximum velocities of rock displacement at the earthquake source may not vary significantly from one earthquake to another, indicating again a notable similarity in rupture processes. Nevertheless these variations are significant in regard to their ground-motion impact and are a significant source of stochastic variability from one event to another.

The slip velocity controlling the high-frequency spectral level in our model can be related to the equivalent Brune stress drop in the Brune (1970) point-source model. Recall that the average (over all azimuths) high-frequency spectral level for the Brune point-source scales as $\Delta\sigma^{2/3}M_0^{1/3}$, where $\Delta\sigma$ is the stress drop (Boore, 1983). Although stress drop has been traditionally used in engineering seismology as a formal parameter controlling the strength of high-frequency radiation, we infer that slip velocity is the real physical quantity that controls high-frequency amplitudes. For example, the same change in stress can lead to either very strong high-frequency radiation, or no high-frequency radiation, depending on the time interval over which it occurred. Clearly, the rate at which stress changes is a key factor; stress drop is simply used as a proxy for the velocity of slip (Beresnev, 2001).

An interesting inference from our finite-fault model is that, for a constant value of maximum slip velocity, the Brune stress drop required to fit the high-frequency spectral level (if the event is modeled as a point source) appears to decrease as moment magnitude increases. Specifically, the average slip velocity of 0.4 m/sec produces a spectral level that, when averaged over all azimuths, requires a Brune point-source stress drop of about 150 bars for **M** 5, 70 bars for **M** 7, and only 25 bars for **M** 8. This may explain the empirical observation of decreasing Brune stress drop with increasing magnitude (Toro *et al.,* 1997). It may also explain why inferred ENA stress drops are typically larger than WNA stress drops; modeled ENA events tend to be lower in magnitude than their WNA counterparts (e.g., **M** ~5 in ENA versus **M** ~7 in WNA).

Conclusions

We conclude that the subfault size that best simulates strong-motion data from 17 well-recorded earthquakes in WNA follows a simple linear relationship, increasing with the moment magnitude of the earthquake in an apparently deterministic manner. The observed trend in WNA is statistically the same as that observed in ENA.

Our results indicate that large earthquakes should be viewed as a sequence of smaller events that comprise the large rupture. The characteristic size of these constituent small events is directly related to the size of the overall rupture, at least in the statistical sense. This conclusion may seem obvious, since the ideas of asperities, or zones that rupture on the faults and are separated by barriers, have long been in use in seismology. What is new and remarkable is the finding that the size of these asperities (or subevents) is unambiguously related to the size of the rupture and that this relationship is regionally independent.

Our inference is supported by other independent studies by Somerville *et al.* (1999) and Aki (1992), in which the characteristic size of the rupture patches on earthquake faults has been determined. Even though these subevents are labeled differently by different authors, depending on the particular model used (subfaults, asperities, or barrier intervals), they seem to reflect the same reality: large earthquakes rupture discretely on a series of subfaults and should not be regarded as single sources. The size of the discrete subevents is directly related to the size of the overall rupture.

The maximum slip velocity on the fault appears to be a stable parameter that varies stochastically over a relatively narrow range. For the 26 events modeled in our study, the maximum slip velocity that we infer lies in the range from 0.25 to 0.60 m/sec. The slip velocities obtained for the WNA earthquakes exhibit an apparent decrease with increasing magnitude, while the ENA earthquakes appear to have randomly distributed slip velocities. If all events are considered together, they exhibit the mean value of slip velocity of 0.40 m/sec with the standard deviation of 0.09 m/sec.

The inferences from this study may have important implications for the prediction of strong ground motions and their uncertainties. Toro *et al.* (1997) distinguished between two fundamentally different types of uncertainty in ground-motion prediction. Epistemic uncertainty is caused by incomplete knowledge of the physical processes (i.e., uncer-

tainty in the true mean) and can in principle be reduced by analyzing more data. On the other hand, aleatory uncertainty is due to the inherent randomness and unpredictability of the specific parameter values of future events (i.e., scatter about the mean) and is thus irreducible. Insufficient knowledge of the mean size of the characteristic rupture zones that form large earthquakes can be classified as epistemic uncertainty. The relationship between subevent size and magnitude derived in this article thus reduces epistemic uncertainty by empirically constraining the subevent size, leaving just aleatory uncertainty representing event-to-event scatter about the mean trend. Similarly, uncertainty in the mean slip velocity can be considered as epistemic uncertainty, while its apparently random variability about the determined mean value is aleatory uncertainty. The findings of this study thus reduce epistemic uncertainty and quantify aleatory uncertainty. The subevent size and slip-velocity parameters are region independent, indicating uniformity in source properties across variable tectonic settings and suggesting that a generic region-independent earthquake source model can be developed.

Acknowledgments

References

Aki, K. (1967). Scaling law of seismic spectrum, *J. Geophys. Res.* **72,** 1217–1231.

Aki, K. (1992). Higher-order interrelations between seismogenic structures and earthquake process, *Tectonophysics* **211,** 1–12.

Aki, K., and P. Richards (1980). *Quantitative Seismology: Theory and Methods,* W. H. Freeman and Company, San Francisco, 932 pp.

Archuleta, R. J., E. Cranswick, C. Mueller, and P. Spudich (1982). Source parameters of the 1980 Mammoth Lakes, California, earthquake sequence, *J. Geophys. Res.* **87,** 4595–4607.

Atkinson, G. M. (1993). Earthquake source spectra in eastern North America, *Bull. Seism. Soc. Am.* **83,** 1778–1798.

Atkinson, G. M., and I. A. Beresnev (1997). Don't call it stress drop, *Seism. Res. Lett.* **68,** 3–4.

Atkinson, G. M., and W. Silva (1997). An empirical study of earthquake source spectra for California earthquakes, *Bull. Seism. Soc. Am.* **87,** 97–113.

Atkinson, G. M., and W. Silva (2000). Stochastic modeling of California ground motions, *Bull. Seism. Soc. Am.* **90,** 255–274.

Berardi, R., M. J. Jiménez, G. Zonno, and M. García-Fernández (2000). Calibration of stochastic finite-fault ground motion simulations for the 1997 Umbria-Marche, Central Italy, earthquake sequence, *Soil Dyn. Earthquake Eng.* **20,** 315–324.

Beresnev, I. A. (2001). What we can and cannot learn about earthquake sources from the spectra of seismic waves, *Bull. Seism. Soc. Am.* **91,** 397–400.

Beresnev, I. A., and G. M. Atkinson (1997). Modeling finite-fault radiation from the ω^n spectrum, *Bull. Seism. Soc. Am.* **87,** 67–84.

Beresnev, I. A., and G. M. Atkinson (1998a). FINSIM: a FORTRAN program for simulating stochastic acceleration time histories from finite faults, *Seism. Res. Lett.* **69,** 27–32.

Beresnev, I. A., and G. M. Atkinson (1998b). Stochastic finite-fault modeling of ground motions from the 1994 Northridge, California, earthquake. I. Validation on rock sites, *Bull. Seism. Soc. Am.* **88,** 1392–1401.

Beresnev, I. A., and G. M. Atkinson (1999). Generic finite-fault model for ground-motion prediction in eastern North America, *Bull. Seism. Soc. Am.* **89,** 608–625.

Bolt, B. A., T. V. McEvilly, and R. A. Uhrhammer (1981). The Livermore Valley, California, sequence of January 1980, *Bull. Seism. Soc. Am.* **71,** 451–463.

Boore, D. M. (1983). Stochastic simulation of high-frequency ground motions based on seismological models of the radiated spectra, *Bull. Seism. Soc. Am.* **73,** 1865–1894.

Boore, D. M., and W. B. Joyner (1997). Site amplifications for generic rock sites, *Bull. Seism. Soc. Am.* **87,** 327–341.

Brune, J. N. (1970). Tectonic stress and the spectra of seismic shear waves from earthquakes, *J. Geophys. Res.* **75,** 4997–5009.

Castro, R. R., A. Rovelli, M. Cocco, M. Di Bona, and F. Pacor (2001). Stochastic simulation of strong-motion records from the 26 September 1997 (*Mw* 6), Umbria-Marche (Central Italy) earthquake, *Bull. Seism. Soc. Am.* **91,** 27–39.

Cockerham, R. S., and E. J. Corbett (1987). The July 1986 Chalfant Valley, California, earthquake sequence: preliminary results, *Bull. Seism. Soc. Am.* **77,** 280–289.

Cohee, B. P., and G. C. Beroza (1994). Slip distribution of the 1992 Landers earthquake and its implications for earthquake source mechanics, *Bull. Seism. Soc. Am.* **84,** 692–712.

Eaton, J. P. (1990). The earthquake and its aftershocks from May 2 through September 30, 1983, in *The Coalinga, California, Earthquake of May 2, 1983,* M. J. Rymer and W. L. Ellsworth (Editors), *U.S. Geol. Surv. Profess. Pap. 1487,* Washington, 113–170.

Fletcher, J., J. Boatwright, L. Haar, T. Hanks, and A. McGarr (1984). Source parameters for aftershocks of the Oroville, California, earthquake, *Bull. Seism. Soc. Am.* **74,** 1101–1123.

Hartzell, S. H. (1978). Earthquake aftershocks as Green's functions, *Geophys. Res. Lett.* **5,** 1–4.

Hartzell, S. (1989). Comparison of seismic waveform inversion results for the rupture history of a finite fault: application to the 1986 North Palm Springs, California, earthquake, *J. Geophys. Res.* **94,** 7515–7534.

Hartzell, S. H., and T. H. Heaton (1986). Rupture history of the 1984 Morgan Hill, California, earthquake from the inversion of strong motion records, *Bull. Seism. Soc. Am.* **76,** 649–674.

Hartzell, S., and M. Iida (1990). Source complexity of the 1987 Whittier Narrows, California, earthquake from the inversion of strong motion records, *J. Geophys. Res.* **95,** 12,475–12,485.

Heaton, T. H. (1982). The 1971 San Fernando earthquake: a double event? *Bull. Seism. Soc. Am.* **72,** 2037–2062.

Heaton, T. H., and S. H. Hartzell (1989). Estimation of strong ground motions from hypothetical earthquakes on the Cascadia subduction zone, Pacific Northwest, *Pageoph* **129,** 131–201.

Hutchings, L. (1994). Kinematic earthquake models and synthesized ground motion using empirical Green's functions, *Bull. Seism. Soc. Am.* **84,** 1028–1050.

Irikura, K. (1983). Semi-empirical estimation of strong ground motions during large earthquakes, *Bull. Disaster Prevention Res. Inst. Kyoto Univ.* **33,** 63–104.

Irikura, K., and K. Kamae (1994). Estimation of strong ground motion in broad-frequency band based on a seismic source scaling model and an empirical Green's function technique, *Ann. Geofis.* **37,** 1721–1743.

Joyner, W. B., and D. M. Boore (1986). On simulating large earthquakes by Green's-function addition of smaller earthquakes, in *Proc. of the Fifth Maurice Ewing Symposium on Earthquake Source Mechanics,* S. Das, J. Boatwright, and C. Scholz (Editors), American Geophysical Union, 269–274.

Kanamori, H. (1979). A semi-empirical approach to prediction of long-period ground motions from great earthquakes, *Bull. Seism. Soc. Am.* **69,** 1645–1670.

Kanamori, H., and D. L. Anderson (1975). Theoretical basis of some empirical relations in seismology, *Bull. Seism. Soc. Am.* **65,** 1073–1095.

Olson, A. H., and R. J. Apsel (1982). Finite faults and inverse theory with applications to the 1979 Imperial Valley earthquake, *Bull. Seism. Soc. Am.* **72,** 1969–2001.

Papageorgiou, A. S., and K. Aki (1983). A specific barrier model for the quantitative description of inhomogeneous faulting and the prediction of strong ground motion. I. Description of the model, *Bull. Seism. Soc. Am.* **73,** 693–722.

Raoof, M., R. B. Herrmann, and L. Malagnini (1999). Attenuation and excitation of three-component ground motion in southern California, *Bull. Seism. Soc. Am.* **89,** 888–902.

Savage, J. C., and W. K. Gross (1995). Revised dislocation model of the 1986 Chalfant Valley earthquake, eastern California, *Bull. Seism. Soc. Am.* **85,** 629–631.

Somerville, P., K. Irikura, R. Graves, S. Sawada, D. Wald, N. Abrahamson, Y. Iwasaki, T. Kagawa, N. Smith, and A. Kowada (1999). Characterizing crustal earthquake slip models for the prediction of strong ground motion, *Seism. Res. Lett.* **70,** 59–80.

Somerville, P., M. Sen, and B. Cohee (1991). Simulations of strong ground motions recorded during the 1985 Michoacán, Mexico and Valparaíso, Chile, earthquakes, *Bull. Seism. Soc. Am.* **81,** 1–27.

Steidl, J. H., R. J. Archuleta, and S. H. Hartzell (1991). Rupture history of the 1989 Loma Prieta, California, earthquake, *Bull. Seism. Soc. Am.* **81,** 1573–1602.

Stein, R. S., and G. Ekström (1992). Seismicity and geometry of a 110-km-long blind thrust fault. II. Synthesis of the 1982–1985 California earthquake sequence, *J. Geophys. Res.* **97,** 4865–4883.

Toro, G. R., N. A. Abrahamson, and J. F. Schneider (1997). Model of strong ground motions from earthquakes in central and eastern North America: best estimates and uncertainties, *Seism. Res. Lett.* **68,** 41–57.

Tumarkin, A. G., and R. J. Archuleta (1994). Empirical ground motion prediction, *Ann. Geofis.* **37,** 1691–1720.

Wald, D. J., and T. H. Heaton (1994). Spatial and temporal distribution of slip for the 1992 Landers, California, earthquake, *Bull. Seism. Soc. Am.* **84,** 668–691.

Wald, D. J., T. H. Heaton, and K. W. Hudnut (1996). The slip history of the 1994 Northridge, California, earthquake determined from strong-motion, teleseismic, GPS, and leveling data, *Bull. Seism. Soc. Am.* **86,** S49–S70.

Wald, D. J., D. V. Helmberger, and T. H. Heaton (1991). Rupture model of the 1989 Loma Prieta earthquake from the inversion of strong-motion and broadband teleseismic data, *Bull. Seism. Soc. Am.* **81,** 1540–1572.

Wells, D. L., and K. J. Coppersmith (1994). New empirical relationships among magnitude, rupture length, rupture width, rupture area, and surface displacement, *Bull. Seism. Soc. Am.* **84,** 974–1002.

Wyss, M., and J. N. Brune (1967). The Alaska earthquake of 28 March 1964: a complex multiple rupture, *Bull. Seism. Soc. Am.* **57,** 1017–1023.

Zeng, Y., J. G. Anderson, and G. Yu (1994). A composite source model for computing realistic strong ground motions, *Geophys. Res. Lett.* **21,** 725–728.

Department of Geological & Atmospheric Sciences
Iowa State University
253 Science I
Ames, Iowa 50011-3212
beresnev@iastate.edu
    (I.A.B.)

Department of Earth Sciences
Carleton University
1125 Colonel By Drive
Ottawa, Ontario K1S 5B6, Canada
gma@ccs.carleton.ca
    (G.M.A.)